High-resolution scanning electron microscopy of an ultracold quantum gas

TATJANA GERICKE, PETER WÜRTZ, DANIEL REITZ, TIM LANGEN AND HERWIG OTT*

Institut für Physik, Johannes Gutenberg-Universität, 55099 Mainz, Germany
*e-mail: ott@uni-mainz.de

Our knowledge of ultracold quantum gases is strongly influenced by our ability to probe these objects. *In situ* imaging combined with single-atom sensitivity is an especially appealing scenario, as it can provide direct information on the structure and the correlations of such systems. For a precise characterization a high spatial resolution is mandatory. In particular, the perspective to study quantum gases in optical lattices makes a resolution well below one micrometre highly desirable. Here, we report on a novel microscopy technique, which is based on scanning electron microscopy and allows for the detection of single atoms inside a quantum gas with a spatial resolution of better than 150 nm. We document the great functionality of this technique by precise density measurements of a trapped Bose–Einstein condensate and the first experimental demonstration of single-site addressability in a submicrometre optical lattice.

Ultracold atoms can be visualized by various techniques. Absorption imaging[1] is the workhorse in most experiments and is typically applied in time of flight to increase the cloud size and reduce the optical density. Whereas phase-contrast imaging[2,3] is well suited for trapped quantum gases, fluorescence imaging[4–9] is particularly attractive as it allows for single-atom detection with almost 100% efficiency. It has been applied to isolated thermal atoms at low densities but has not yet been extended to single-atom detection in quantum gases. The best achievable resolution of these optical techniques is ultimately limited by half the wavelength of the used light field—in practice, the best reported resolution is about 1 μm (ref. 5). Direct particle detection of metastable atoms in time of flight[10,11] and outcoupling of single atoms from a condensate with a radio-frequency field[12] are alternative techniques that have been developed. However, they either cannot be applied to trapped samples[10,11] or are restricted to one spatial dimension[12]. Although each of these techniques has its specific advantages and applications, a versatile *in situ* detection of single atoms in a quantum gas is lacking. Moreover, a spatial resolution of below 1 μm, which opens the intriguing perspective to resolve single sites in a submicrometre optical lattice, has not yet been achieved.

WORKING PRINCIPLE

In our experiment we have transferred the principles of scanning electron microscopy to the detection of ultracold atoms (Fig. 1). A focused electron beam with 6 keV electron energy, a full-width-at-half-maximum (FWHM) diameter of 100–150 nm and a current of 10–20 nA is scanned across a Bose–Einstein condensate of rubidium atoms, which is prepared in an optical dipole trap[13]. The atoms are ionized by electron impact ionization, extracted with an electrostatic field and subsequently detected by an ion detector. The small diameter of the electron beam ensures a high spatial resolution, whereas the ion detection provides single-atom sensitivity. The total ionization cross-section for rubidium at 6 keV electron energy is $\sigma_{\mathrm{ion}} = 3.5 \times 10^{-17}\,\mathrm{cm}^2$ (ref. 14) and represents
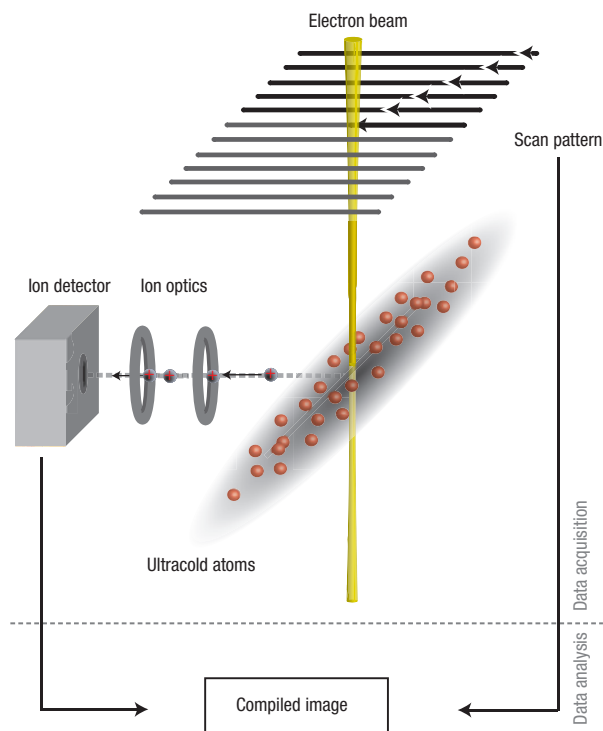
40% of all scattering events[15,16]. Elastic and inelastic electron–atom collisions constitute the remaining events and lead to atom loss with no detectable signal. As the cross-section is eight orders of magnitude smaller than the absorption cross-section of a resonant photon, the atomic cloud is optically thin for the electron beam. For typical parameters, only one out of 500,000 incident electrons undergoes a collision.

IMAGING A BOSE–EINSTEIN CONDENSATE

When exposed to the electron beam, the probability of detection of an atom at a position $\{x, y\}$ is given by (see the Methods section)

$$P(x, y) = \frac{I}{e}\sigma_{\mathrm{ion}}\Delta t\,\eta_{\mathrm{det}}N \int \mathrm{d}z\,|\phi(x, y, z)|^2. \qquad (1)$$
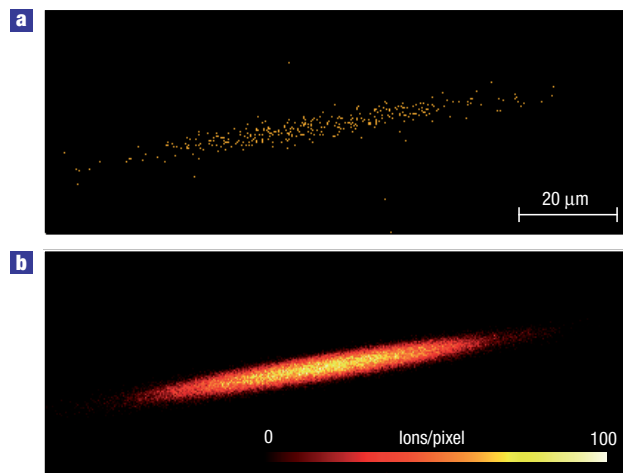
Here, I is the electron-beam current, e is the electron charge, Δt is the pixel dwell time of the electron beam, η_{det} is the detector efficiency, $\int \mathrm{d}z\,|\phi(x, y, z)|^2$ denotes the column density of the atom's wavefunction along the propagation direction of the electron beam (z-direction) and N is the number of atoms in the single-particle state. In Fig. 2a we show a scanning electron microscope image of a Bose–Einstein condensate. For our experimental parameters, a fraction of 350 atoms is detected (the total number of atoms in the condensate is about 100,000). In a Bose–Einstein condensate all atoms occupy the same quantum state and the many-body wavefunction ψ separates into the product of N identical single-particle wavefunctions $\psi(\mathbf{x}_1, \ldots, \mathbf{x}_N) = \prod_{i=1}^{N} \phi(\mathbf{x}_i)$, with N being the number of atoms in the condensate. Therefore, the interpretation of the image involves quantum-mechanical concepts: as the single-particle wavefunction ϕ extends over the whole atomic cloud, the spatially resolved detection of an atom must be understood as a projective measurement in position space. As a consequence, the retrieved image is intrinsically probabilistic. This is in contrast to almost all microscopy images showing the distribution of individual atoms, as

Electron beam

Scan pattern

Ion detector   Ion optics

Ultracold atoms

Compiled image

Data acquisition

Data analysis

Figure 1 Working principle. The atomic ensemble is prepared in an optical dipole trap. An electron beam with variable beam current and diameter is scanned across the cloud. Electron impact ionization produces ions, which are guided with an ion optical system towards a channeltron detector. The ion signal together with the scan pattern is used to compile the image.

20 μm

0   Ions/pixel   100

Figure 2 Electron microscope images of a trapped Bose–Einstein condensate. a, An image of a [87]Rb condensate. The image has 400×150 pixels with a pixel size of $300\,nm \times 300\,nm$. Each pixel was illuminated for $2\,\mu s$ with the electron beam (140 nm FWHM beam diameter). Every dot corresponds to a detected atom. In total, 350 ions were collected during the exposure. The condensate contains about 10^5 atoms and the oscillation frequencies in the dipole trap are $\nu_a = 12\,Hz$ ($\nu_\rho = 170\,Hz$) in the axial (radial) direction. **b**, The sum over 300 images. Each image was taken in a separate experimental run.

in these cases the location of the atoms is already fixed before their detection. Another important aspect is related to the Heisenberg uncertainty principle. During the detection process, the atom is coupled to a probe (in our case an electron beam) and energy as well as momentum can be exchanged between them. Consequently, the localization of an atom within a range Δx enforces a momentum spread of $\Delta p \geq \hbar/(2\Delta x)$. If Δx is smaller than the extension of the wavefunction ϕ, substantial momentum transfer is unavoidable and the detected atom is no longer part of the condensate, regardless of the specific experimental realization. Hence, the ionization of the atoms in our scheme does not constitute a serious limitation or drawback. It is even advantageous because it helps to rapidly extract the reaction products from the remaining system, keeping possible perturbations small.

Whether the image in Fig. 2a is indeed a probabilistic selection of the full atomic distribution according to equation (1) can be checked by summing over many images (Fig. 2b) and comparing them with a theoretical density profile. The profile is derived from the so-called semi-ideal model[17–19], which describes a bimodal distribution at finite temperature. Whereas the condensate part is obtained from a numerical solution of the three-dimensional Gross–Pitaevskii equation, the thermal component is modelled as a non-interacting gas in an effective potential, taking into account the repulsion of the thermal atoms by the condensed atoms (see Methods section). The comparison with our data (Fig. 3a,b) shows very good agreement over the whole extension of the cloud including the wings of thermal atoms. This not only gives indirect evidence of the repulsion between the condensate fraction and the thermal component in the trap (Fig. 3b, inset), but also confirms that the image shown in Fig. 2a shows a probabilistic selection of atoms.
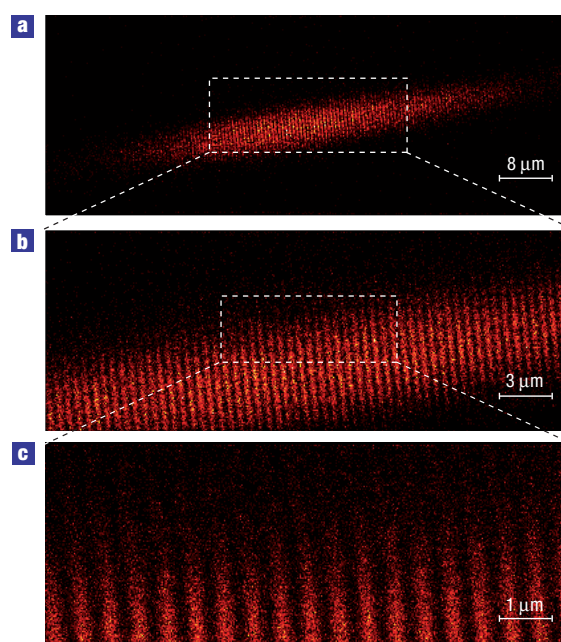
ESTIMATED DENSITY DISTRIBUTION

In Fig. 2b we have summed over 300 individual images, corresponding to an overall number of processed events that is comparable to the total number of atoms in the condensate. The analysis in Fig. 3a,b therefore gives an impression of how accurately the shape of the condensate would be determined if all atoms were detected in an idealized experiment. As the effective number of detected atoms per run is only 350 on average, the question of how much information can be extracted from a single image arises. To answer this we apply a recently reported method for the reconstruction of a probability density from discrete experimental data[20]. This approach avoids the use of histograms and directly evaluates the cumulated data with the help of a Fourier expansion. It does not require previous knowledge of the shape of the distribution. The estimated axial density distribution for the image in Fig. 2a is shown in Fig. 3c. The shape in the centre is well reproduced and only the wings of the distribution show larger deviations due to poor statistics. Processing all images in the same manner and evaluating their FWHM, we find an average of $50.5 \pm 2.5\,\mu m$. This is compatible with an FWHM of $48.9\,\mu m$ obtained from the theoretical model in Fig. 3a. Hence, the precision to which the size of the condensate is determined in a single image is 5%. The necessary extent of data acquisition therefore depends on the specific application. Substantial averaging as done in Fig. 2b is required only if very fine structures such as the wings of a thermal cloud or the precise shape of the density distribution are under investigation.

Comparing the condensate with and without exposure to the electron beam (absorption images in the inset of Fig. 3a), we do not find any significant difference, apart from a reduction in atom number by about 7%. These losses are composed of two contributions: primary electron–atom collisions and secondary collisions of the primary reaction products. We find that every scattered atom or produced ion kicks off on average one more atom. In all these collisions the energy transfer is much larger than the
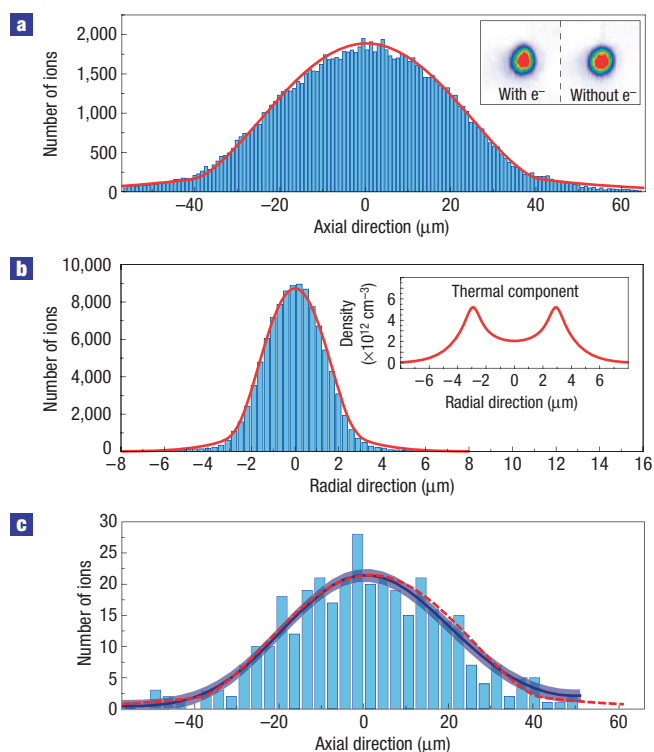
Figure 3 Analysis of the Bose–Einstein condensate. a, The axial distribution of the condensate shown in Fig. 2b, integrated in the radial direction. The experimental data (blue columns, 900 nm bin size) are compared with a bimodal distribution (red line) calculated in the semi-ideal model for a total atom number of $N = 115,000$ and a temperature of $T = 80$ nK. The condensate fraction is 80%. The inset shows absorption images of the condensate after 15 ms time of flight with and without exposure to the electron beam. The number of atoms after exposure is reduced by 7% on average. **b**, The distribution in the radial direction (300 nm bin size). In the inset we have plotted the radial density of the thermal component in the trap centre as calculated from the model. The minimum is due to the repulsion from the condensate fraction. **c**, The estimated density distribution in the axial direction for the single-shot image in Fig. 2a (blue line). The data (columns) have been binned over 3 μm. The blue shaded area indicates the uncertainty of the estimated distribution. For comparison, the red dashed line shows the solution of the theoretical model (the same as in **a**).

Figure 4 Images of a Bose–Einstein condensate loaded in a one-dimensional optical lattice. a–c, The lattice, which is created by two laser beams (wavelength $\lambda = 850$ nm) intersecting at 90°, has a period of $l = 600$ nm. Each image is the sum of 50 individual images. The pixel size is 200 nm × 200 nm (**a**), 75 nm × 75 nm (**b**) and 25 nm × 25 nm (**c**). The lattice depth was 20 recoil energies E_r ($E_r = \pi^2 \hbar^2 / (2ml^2)$, with m being the rubidium mass) and the FWHM diameter of the electron beam was 95 nm.

depth of the optical potential and all scattered particles can escape from the trap. Essentially, no energy is deposited in the cloud, as we observe an additional heating of merely 5 nK after exposure to the electron beam. Thus, the perturbation caused by the detection process is very small. If not, the scanning speed could be made larger than the speed of sound in the condensate, providing an effectively unperturbed cloud during the whole imaging sequence. According to equation (1), high imaging speed is associated with a reduced signal and a convenient setting of the imaging parameters has to be chosen for each application. Most detected ions are singly charged (80%), but we also find higher charged states of up to Rb^{7+} resulting from inner-shell ionization. Only one out of 50 detected events is due to background gas ionization or dark counts, which results in a high signal-to-noise ratio, as shown by Fig. 2. Taking into account a detector efficiency of 30%, the total efficiency for our detection scheme is currently limited to 12%. It could be increased by a more efficient ion detector and additional photoionization of inelastically scattered atoms. We estimate that a total detection efficiency of more than 50% could be feasible.

The small perturbation of the system in combination with a high detection efficiency could make it possible to take several images of the same condensate, thus allowing for a direct observation of the dynamical evolution of an individual system.

ONE-DIMENSIONAL OPTICAL LATTICE

To characterize the resolution of our imaging technique, we have loaded the condensate in a one-dimensional optical lattice with 600 nm lattice period. A sequence of electron microscope images with increasing resolution is shown in Fig. 4a–c. The periodic structure of the potential is clearly resolved with high contrast. The atomic density in each lattice site is radially symmetric, with a diameter of 6 μm and a thickness of 300 nm, and documents the large depth of focus of the electron optical imaging system.

One of the most intriguing properties of a Bose–Einstein condensate is its macroscopic phase coherence. In a periodic potential the phase coherence can be easily verified by interference experiments. An absorption image of the condensate after a ballistic expansion of 15 ms is shown in the inset of Fig. 5a. The image was taken after illumination with the electron beam, and the appearance of the characteristic diffraction peaks demonstrates that the partial measurement of a subset of atoms does not destroy the coherence of the remaining system. Furthermore, it is an example for a complementary measurement in position and momentum space on a single many-body quantum system. For a quantitative analysis we compare the integrated line scans with the Bloch wavefunction that describes the ground state of non-interacting atoms in the lattice potential (Fig. 5a,b). The periodic structure and the shape of the individual on-site wave function are well reproduced for
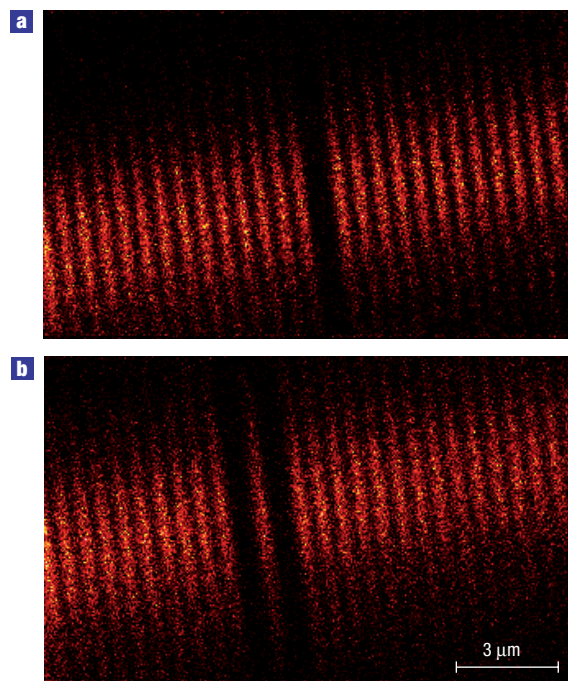
3
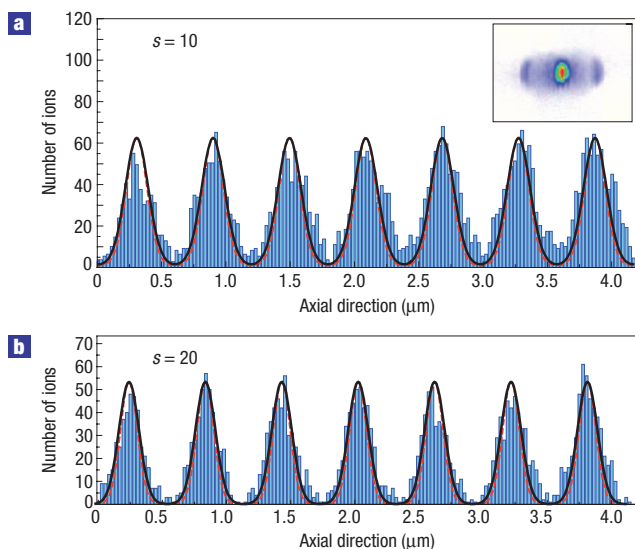
Figure 5 Ground state of a Bose–Einstein condensate in a one-dimensional optical lattice. **a,b**, The graphs show integrated line scans for a lattice depth of $s = 10$ (**a**) and $s = 20$ (**b**), where s measures the lattice depth in units of the recoil energy. The blue columns are the experimental data, which are compared with a theoretical model (black line) based on the ground state in the lattice potential (red dashed line) convolved with a Gaussian electron-beam profile with 95 nm FWHM diameter. An absorption image after 15 ms time of flight (inset in **a**) reveals that the phase coherence of the condensate is preserved after exposure to the electron beam.

Figure 6 Single-site addressability. We first remove atoms from the optical lattice, pointing the electron beam at the specific sites for 35 ms. Thereafter the image is taken (200×325 pixels, 50 nm pixel size, 2 μs pixel dwell time). **a**, A single emptied site (sum over 127 images). The lattice depth of 18 recoil energies is enough to suppress refilling of the lattice site. **b**, The preparation of an isolated site (sum over 142 images).

both data sets. Together with the observed interference pattern both the density distribution and the relative quantum-mechanical phase are determined, and thus the Bloch wavefunction is fully characterized. Eventually, we conclude from the good agreement that our imaging technique achieves a spatial resolution of better than 150 nm (see the Methods section).

SINGLE-SITE ADDRESSABILITY

Ultracold quantum gases in optical lattices[21–23] have triggered a lot of interest owing to the close connection to solid-state systems and the perspective of possible applications in quantum simulation[24] and quantum information processing[25]. One general difficulty in this research field is the addressability in these systems, which has so far been demonstrated only for thermal atoms in a lattice with 5 μm period[26]. Not only a site-selective read-out but also a manipulation of single lattice sites is essential in this context. Here, we demonstrate the spatially resolved dissipative manipulation of an ultracold quantum gas in a one-dimensional optical lattice. In the experiment we first load a Bose–Einstein condensate in a deep optical lattice (18 recoil energies) and point the electron beam at a specific site for 35 ms to remove the atoms. As the atoms are free to move in the radial direction we move the electron beam across only the central part of the site. After the preparation stage the atomic distribution is imaged as described before. The optical lattice shows long-term drifts with respect to the field of view of the electron beam and we find a typical drift of one lattice site per hour. Therefore, for long data acquisition times it may occur that during the preparation stage the electron beam points in between two lattice sites, thus partially emptying both of them. We compensate for this effect, carrying out a phase analysis of each individual image. If the position of the lattice sites is found to deviate more

than is acceptable from the ideal position (we tolerate $\pm l/4$, where l is the lattice constant) the image is discarded. The results of two different scenarios are shown in Fig. 6. In the first image we have emptied a single lattice site. The data clearly document that this can be accomplished without affecting the neighbouring lattice sites. The second image shows the preparation of an isolated lattice site. Again, this can be done without additional losses in the non-addressed sites. This is possible because the electron beam is much smaller than the spacing between the lattice sites.

OUTLOOK

In future experiments, we plan to study the ensuing tunnelling dynamics after the dissipative manipulation. Both the refilling of a hole and the spread of an isolated site are interesting scenarios, which will give more insight into the microscopic physics of ultracold quantum gases in optical lattices. The applied scheme is an important step towards tailored quantum systems and the preparation of mesoscopic atomic ensembles. With the implementation of a second optical lattice, the extension to two-dimensional arrays of lattice sites is straightforward. Ultimate control over the occupancy of the sites can be achieved by starting from a Mott insulator state in a three-dimensional optical lattice[21] and emptying all but one lattice plane perpendicular to the electron beam. This can be accomplished, for example, by a magnetic-field gradient in combination with a microwave transition to a different hyperfine ground state and subsequent removal of the transferred atoms with a resonant laser beam.

The combination of high spatial resolution with *in situ* detection will open up new possibilities for the preparation,

the manipulation and the characterization of ultracold quantum gases. The bonus of single-atom sensitivity, which has not yet been exploited in this work, will provide new means for the measurements of spatial and temporal correlations in trapped quantum gases[27–29]. Previous experimental work on correlations in trapped[30] and expanding[11,31,32] gases has already demonstrated the high potential of such measurements. The local interaction of the electron beam with the atomic ensemble also constitutes a new experimental platform for the study of dissipative processes in many-body quantum systems. In future experiments, the magnetic field of the electron beam might be used even to coherently manipulate single atoms in optical lattices.

METHODS

DETECTION PROBABILITY

An atom that is located in the centre of a Gaussian electron beam with a radial current density of $j(\rho) = j_0 \exp(-\rho^2/2\rho_0^2)$ has a lifetime against electron impact of $\tau = e/(j_0\sigma_{tot})$. Here, $j_0 = I/(2\pi\rho_0^2)$ is the current density in the beam centre, ρ_0 is the σ-width of the beam, and $\sigma_{tot} = 9 \times 10^{-17}$ cm^2 is the total electron scattering cross-section for rubidium at 6 keV electron energy. For typical beam parameters ($I = 23$ nA, FWHM $= 140$ nm, corresponding to $\rho_0 = 58$ nm) we obtain $\tau \approx 17$ µs. If the pixel dwell time Δt is much smaller than τ, the probability of a scattering event (ionization, elastic or inelastic scattering) is given by

$$w = 1 - e^{-\frac{\Delta t}{\tau}} \approx \frac{\Delta t}{\tau} = \frac{j_0}{e}\sigma_{tot}\Delta t.$$

If the atom is described by a wavefunction $\phi(x,y,z)$ and if we assume that the beam is much smaller than the extension of the wavefunction, the probability of a scattering event at the position $\{x,y\}$ is given by

$$w(x,y) = \frac{I}{e}\sigma_{tot}\Delta t \int dz\, |\phi(x,y,z)|^2. \quad (2)$$

Multiplying equation (2) by the ion production efficiency $\sigma_{ion}/\sigma_{tot}$, the detector efficiency η_{det} and the total number of atoms gives equation (1) of the main text.

BIMODAL DISTRIBUTION

For a given number of condensed atoms N_0 we numerically solve the Gross–Pitaevskii equation

$$\left[-\frac{\hbar^2}{2m}\nabla + V_{ext}(\mathbf{r}) + g|\psi(\mathbf{r})|^2 \right]\psi(\mathbf{r}) = \mu\psi(\mathbf{r}) \quad (3)$$

using an imaginary time-propagation algorithm. The external potential is cylindrically symmetric and has the form $V_{ext}(\rho,z) = \frac{1}{2}m(\omega_\rho^2\rho^2 + \omega_a^2 z^2)$, where z denotes the axial direction of the condensate, $\omega_a = 2\pi \times 12$ Hz ($\omega_\rho = 2\pi \times 170$ Hz) is the axial (radial) oscillation frequency of the dipole trap, μ is the chemical potential and $g = 4\pi\hbar^2 a/m$ is the coupling constant. For the s-wave scattering length we use a value of $a = 101\, a_0$, with a_0 being the Bohr radius. In our experiment we produce a spinor condensate in the $|F = 1\rangle$ ground state of rubidium. For the model presented here we ignore the spinor nature because the difference in the scattering lengths for the $F = 0$ and 2 scattering channels is only 1% (ref. 33). The condensate wavefunction is normalized to the total number of condensed atoms, $N_0 = \int d^3x\, |\psi(\mathbf{r})|^2$. The numerical solution of equation (3) is used to model an effective potential for the thermal component

$$V_{eff}(\mathbf{r}) = V_{ext}(\mathbf{r}) + 2g|\psi(\mathbf{r})|^2.$$

The density distribution of the thermal component is then given by

$$n_{th}(\mathbf{r}) = \lambda_{th}^{-3} g_{3/2}(z)$$

with a modified fugacity

$$z = \exp[-(V_{eff}(\mathbf{r}) - \mu)/k_B T].$$

and $g_{3/2} = \sum_{k=1}^\infty z^k/k^{3/2}$. Here, $\lambda_{th} = \sqrt{2\pi\hbar^2/mk_B T}$ is the thermal de Broglie wavelength and k_B is the Boltzmann constant. The number of atoms in the thermal component is given by $N_{th} = \int d^3x\, n_{th}(\mathbf{r})$ and the total number of atoms is $N = N_0 + N_{th}$.

SPATIAL RESOLUTION

The size of the electron beam can be determined independently by scanning the beam across a sharp edge of a movable test target which is implemented in the vacuum chamber. We define the resolution as the distance between two neighbouring pointlike scatterers where the signal intensity in between drops to 75%. This definition is the analogue to the Rayleigh criterion in optics and for our system translates into a resolution of $d = 1.18$ FWHM, assuming a Gaussian beam profile. The electron beam used for the measurement in Figs 4 and 5 of the main text has a diameter of 95 nm FWHM, corresponding to a resolution of 115 nm. The good agreement between the experimental line scan and the theoretical model in Fig. 5 proves that a similar resolution is achieved for the electron microscope images of ultracold atoms.

References

1. Ketterle, W., Durfee, D. & Stamper-Kurn, D. *Bose–Einstein Condensation in Atomic Gases, Proc. Int. School of Physics Enrico Fermi* (IOS Press, 1999).
2. Andrews, M. *et al.* Direct, non-destructive imaging of a Bose condensate. *Science* **273**, 84–87 (1996).
3. Shin, Y., Zwierlein, M., Schunck, C., Schirotzek, A. & Ketterle, W. Observation of phase separation in a strongly interacting imbalanced Fermi gas. *Phys. Rev. Lett.* **97**, 030401 (2006).
4. Hu, Z. & Kimble, H. Observation of a single atom in a magneto-optical trap. *Opt. Lett.* **19**, 1888–1890 (1994).
5. Schlosser, N., Reymond, G., Protsenko, I. & Grangier, P. Sub-Poissonian loading of single atoms in a microscopic dipole trap. *Nature* **411**, 1024–1027 (2001).
6. Kuhr, S. *et al.* Deterministic delivery of a single atom. *Science* **293**, 278–280 (2001).
7. Schrader, D. *et al.* Neutral atom quantum register. *Phys. Rev. Lett.* **93**, 150501 (2004).
8. Teper, I., Lin, Y. & Vuletic, V. Resonator-aided single-atom detection on a microfabricated chip. *Phys. Rev. Lett.* **97**, 023002 (2006).
9. Nelson, K., Li, X. & Weiss, D. Imaging single atoms in a three-dimensional array. *Nature Phys.* **3**, 556–560 (2007).
10. Schellekens, M. *et al.* Hanbury Brown Twiss effect for ultracold quantum gases. *Science* **310**, 648–651 (2005).
11. Jeltes, T. *et al.* Comparison of the Hanbury Brown–Twiss effecct for bosons and fermions. *Nature* **445**, 402–405 (2007).
12. Öttl, A., Ritter, S., Köhl, M. & Esslinger, T. Correlations and counting statistics of an atom laser. *Phys. Rev. Lett.* **95**, 090404 (2005).
13. Gericke, T., Würtz, P., Reitz, D., Utfeld, C. & Ott, H. All-optical formation of a Bose–Einstein condensate for applications in scanning electron microscopy. *Appl. Phys. B* **89**, 447–451 (2007).
14. Bartlett, P. L. & Stelbovics, A. T. Electron-impact ionization cross sections for elements z = 1 to 54. *At. Data Nuc. Data Tab.* **86**, 235–265 (2004).
15. Schappe, R., Feng, P., Anderson, L., Lin, C. & Walker, T. Electron collision cross-sections measured with the use of a magneto-optical trap. *Europhys. Lett.* **29**, 439–444 (1995).
16. Schappe, R., Walker, T., Anderson, L. W. & Lin, C. C. Absolute electron-impact ionization cross section measurements using a magneto-optical trap. *Phys. Rev. Lett.* **76**, 4328–4331 (1996).
17. Minguzzi, A., Conti, S. & Tosi, M. P. The internal energy and condensate fraction of a trapped interacting Bose gas. *J. Phys. Condens. Matter* **9**, L33–L38 (1997).
18. Naraschewski, M. & Stamper-Kurn, D. M. Analytical description of a trapped semi-ideal Bose gas at finite temperature. *Phys. Rev. A* **58**, 2423–2426 (1998).
19. Gerbier, F. *et al.* Experimental study of the thermodynamics of an interacting trapped Bose–Einstein condensed gas. *Phys. Rev. A* **70**, 013607 (2004).
20. Berg, B. A. & Harris, R. C. From data to probability densities without histograms. *Comput. Phys. Commun.* **179**, 443–448 (2008).
21. Greiner, M., Mandel, O., Esslinger, T., Hänsch, T. W. & Bloch, I. Quantum phase transition from a superfluid to a Mott insulator in a gas of ultracold atoms. *Nature* **415**, 39–44 (2002).
22. Mandel, O. *et al.* Controlled collisions for multiparticle entanglement of optically trapped atoms. *Nature* **425**, 937–940 (2003).
23. Morsch, O. & Oberthaler, M. Dynamics of Bose–Einstein condensates in optical lattices. *Rev. Mod. Phys.* **78**, 179–215 (2006).
24. Bloch, I. Quantum Gases. *Science* **319**, 1202–1203 (2008).
25. Raussendorf, R. & Briegel, H. J. A one-way quantum computer. *Phys. Rev. Lett.* **86**, 5188–5191 (2001).
26. Scheunemann, R., Cataliotti, F. S., Hänsch, T. W. & Weitz, M. Resolving and addressing atoms in individual sites of a CO$_2$-laser optical lattice. *Phys. Rev. A* **62**, 051801 (2000).
27. Naraschewski, M. & Glauber, R. J. Spatial coherence and density correlations of trapped Bose gases. *Phys. Rev. A* **59**, 4595–4607 (1999).
28. Kheruntsyan, K., Gangardt, D., Drummond, P. & Shlyapnikov, G. V. Finite-temperature correlations and density profiles of an inhomogeneous interacting one-dimensional Bose gas. *Phys. Rev. A* **71**, 053615 (2005).
29. Sykes, A. G. *et al.* Spatial nonlocal pair correlations in a repulsive 1d Bose gas. *Phys. Rev. Lett.* **100**, 160406 (2008).
30. Estève, J. *et al.* Observations of density fluctuations in an elongated Bose gas: Ideal gas and quasicondensate regimes. *Phys. Rev. Lett.* **96**, 130403 (2006).
31. Greiner, M., Regal, C. A., Stewart, J. T. & Jin, D. S. Probing pair-correlated fermionic atoms through correlations in atom shot noise. *Phy. Rev. Lett.* **94**, 110401 (2005).
32. Fölling, S. *et al.* Spatial quantum noise interferometry in expanding ultracold atom clouds. *Nature* **434**, 481–484 (2005).
33. Van Kempen, E. G. M., Kokkelmans, S. J. J. M. F., Heinzen, D. J. & Verhaar, B. J. Interisotope determination of ultracold rubidium interactions from three high-precision experiments. *Phys. Rev. Lett.* **88**, 093201 (2002).

Author information
Reprints and permissions information is available online at http://npg.nature.com/reprintsandpermissions. Correspondence and requests for materials should be addressed to H.O.